ACS APPLIED MATERIALS & INTERFACES

www.acsami.org Research Article

Synthesis of Metastable Calcium Carbonate Using Long-Chain Bisphosphonate Molecules

Trinh Thao My Nguyen, Shan Hazoor, Thanh Vuong, LeMaur Kydd, Ian Shortt, Frank W. Foss, Jr.,* and Erika La Plante*

Cite This: *ACS Appl. Mater. Interfaces* 2024, 16, 30567−30579 **Read Online**

ACCESS | Metrics & More | Article Recommendations | Supporting Information

ABSTRACT: Cementation in construction materials primarily relies on the aqueous precipitation of minerals such as carbonates and silicates. The kinetics of nucleation and growth play a critical role in the development of strength and durability, yet our understanding of the kinetic controls governing phase formation and porosity reduction in cements remains limited. In this study, we synthesized bisphosphonate molecules with varying alkyl chain lengths and functional groups to investigate their impact on calcium carbonate precipitation. Through conductivity measurements, infrared spectroscopy, and thermogravimetric analysis, we uncovered the selective formation of polymorphs and the specific incorporation of these molecules within the carbonate matrix. Further, in situ atomic force microscopy revealed that these molecules influenced the morphology of the precipitates, indicating a possible effect on the ionic organization through sorption mechanisms. Interestingly, amorphous calcium carbonate (ACC), when formed in the presence of bisphosphonates, showed metastability for at least seven months without inhibiting further calcium carbonate precipitation. Our research sheds light on the diverse mechanisms by which organic additives can modify mineral nucleation and growth, offering valuable insights for the control and enhancement of carbonate-based cementation processes.

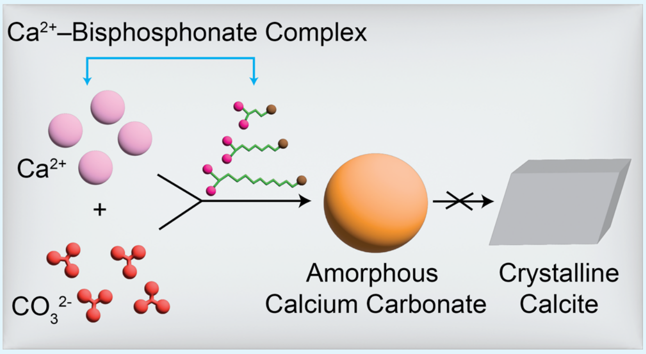

KEYWORDS: *Polymorph selection, atomic force microscopy, alkyl chain, vaterite, amorphous calcium carbonate, metastability*

1. INTRODUCTION

The production of cement accounts for approximately 8% of global carbon dioxide (CO_2) emissions.[1,2] To mitigate the environmental impact of ordinary Portland cement (OPC) production, carbonate rocks such as limestone have been utilized as an admixture,[3] and cements that cure by capturing CO_2 in the form of calcium carbonate ($CaCO_3$) have been employed.[4] $CaCO_3$ exists in a variety of polymorphs, including amorphous $CaCO_3$ (ACC)—the least stable polymorph, two hydrated forms: monohydrocalcite ($CaCO_3 \cdot H_2O$) and ikaite ($CaCO_3 \cdot 6H_2O$), and three anhydrous forms: vaterite, aragonite, and calcite. The anhydrous crystalline phases have been extensively studied; among them, aragonite and calcite are the most thermodynamically stable and widely occurring in nature.[5,6] However, because of its rhombohedral morphology, calcite is typically not preferred as a cement binder.[7] In contrast, vaterite consists of small spherical crystallites that enhance the specific surface area, making it more desirable for certain cement applications.[7]

Calcium carbonate ($CaCO_3$) is produced in nature by various organisms, including mollusks and echinoderms. Some of these organisms generate metastable ACC as a precursor to more stable forms like aragonite or calcite, while others can stabilize ACC.[8] The transformation from ACC to calcite typically involves the rapid dehydration and reorganization of the internal structure. This process forms an intermediate phase, vaterite, which then transforms into calcite.[9] Numerous studies have successfully synthesized vaterite by manipulating various parameters such as pH, temperature, reaction time, solvent, or additives,[10−14] as well as through different synthesis methods such as the carbonation of Ca^{2+}-containing solutions or the mixing of two aqueous salt solutions.[13−15] Despite vaterite's metastability, it has been demonstrated to be the primary phase formed during accelerated carbonation under high CO_2 concentrations.[15] The subsequent conversion of vaterite to needle-like aragonite, noted for its increased hardness and density, enhances connectivity within the matrix and contributes to strength gain in the material.[7,16]

Received: March 15, 2024
Revised: May 14, 2024
Accepted: May 19, 2024
Published: June 3, 2024

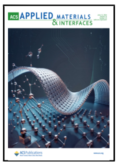

https://doi.org/10.1021/acsami.4c04218

In the shells and skeletons of many organisms, negatively charged amino acids are prevalent and play a crucial role in the growth and selection of polymorphs of $CaCO_3$ during biomineralization.[17,18] Consequently, the kinetics of $CaCO_3$ precipitation in the presence of aspartic acid, other amino acids, and peptides has been widely studied.[19−23] High concentrations of aspartic acid and polyaspartic acid, for example, have been shown to stabilize ACC; however, their doubly negative charge at neutral pH allows them to attach to the growing crystal faces, inhibiting further growth.[17,19,24] Amino acids with nonpolar side chains, such as leucine (with an aliphatic side chain) and tyrosine (with a phenol side chain), exhibit interesting effects: the formation of calcite is disfavored at low amino acid concentrations but becomes favorable at high concentrations.[23] Amino acids and proteins also affect the formation of $CaCO_3$ through interactions with Ca^{2+} and CO_3^{2-} ions, thus affecting equilibrium and inducing supramolecular effects.[25]

Despite substantial knowledge of the precipitation of crystalline and amorphous $CaCO_3$ in the presence of organic ligands, several key research questions remain. These include the mechanisms of ACC stabilization and the identification of specific structures and functional groups in organic ligands that stabilize particular $CaCO_3$ phases. In previous studies, the amino acids examined often possessed multiple variable characteristics (simultaneously), such as structure, functional group, degree of polymerization, or chain length, complicating the understanding of their individual effects.

In this study, we investigate the effect of synthetic bisphosphonates on the kinetics of $CaCO_3$ precipitation. Bisphosphonates are robust organic molecules that mimic the properties of amino acids and proteins, such as carboxylic acids and phosphonates, and form relatively strong interactions with calcium ions.[26] Notably, bisphosphonates act as specific inhibitors of bone resorption and are commonly prescribed for the treatment of osteoporosis.[27] A series of bisphosphonates was synthesized to explore the impact of hydrophobicity, terminal functional group, and charge state of bisphosphonate side chains on the growth kinetics of $CaCO_3$. To understand the relationship between molecular-scale structures and their function, we characterized the precipitation rates and products through conductivity measurements, thermogravimetric analysis, and infrared (IR) spectroscopy. The findings provide insights into pathways for controlling the chemical and mechanical properties of carbonate phases in cementitious materials.

2. MATERIALS AND METHODS

2.1. Synthesis of Bisphosphonate Molecules. The synthesis of molecules in this study (see Figure 1) commenced with commercially available tetraethyl methylenebisphosphonate (compound **2** in Figure 1), which was utilized as-is for discovery-scale syntheses. For larger, multigram-scale syntheses, tetraethyl methylenebisphosphonate (compound **2**) was produced from cost-effective dichloromethane and diethyl phosphite (compound **1**).[28] The common starting material (compound **2**) underwent base treatment with NaH and alkylation with various lengths of alkyl W-bromocarboxylates (compounds **3a**−**c**) to create ester-substituted bisphosphonates (**4a**−**c**) with three, seven, or eleven carbons in their backbone. The carboxylic acids were revealed by saponification of the ester group to yield compounds **5a**−**c**. The tetraethyl bisphosphonates were deprotected by treatment with different equivalents of bromotrimethylsilane, followed by methanol solvolysis, to yield the final bisphosphonic acids with carboxylic acid side chains (compounds **6a**−**c**) with satisfactory yields. The intermediate acids (compounds **5a**−**c**) could be conveniently reduced with borane dimethyl sulfide and then similarly deprotected to produce the final bisphosphonic acids with hydroxyl side chains (compounds **7a**−**c**). An alkyl-substituted bisphosphonate—created for comparative purposes with compounds **6c** and **7c**—was synthesized through alpha-carbon substitution using a base and 1-bromodecane, resulting in good yield, followed by tetraethyl deprotection to obtain the final product (compound **8**). The molecular structures and purities were verified by using ^1H, $^{13}C\{^1H\}$, and ^{31}P nuclear magnetic resonance (NMR) spectroscopy, high-resolution mass spectrometry, infrared spectroscopy, and melting point determinations. Detailed methods and complete analytical data for all compounds and their intermediates are found in the Supporting Information (Figures S1−S44). Special note should be made of the unusually large equivalents of bromotrimethylsilane required for deprotecting the shorter, more polar bisphosphonates, compounds **6a** and **7a**.

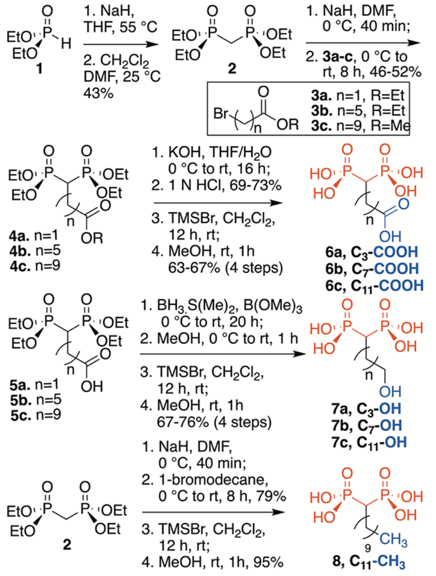

Figure 1. Schematic of synthesis of bisphosphonate molecules: (**1**) diethyl phosphite, (**2**) tetraethyl methylenebisphosphonate, (**3**) W-bromocarboxylates, (**4**) ester-substituted bisphosphonates, (**5**) tetraethyl bisphosphonate, (**6a**−**c**) carboxylic acid, (**7a**−**c**) alcohol, (**8**) and alkyl bisphosphonates.

2.2. Computational Modeling of Organic Complexation. Density functional theory (DFT) was used to predict the low-energy conformations of bisphosphonates when they are bound to Ca^{2+}. The energy-minimized geometries and frequency analyses were computed in the ground state using the M06-2X[29] exchange-correlation functional with the 6-31G(d) basis set. This basis set was augmented with a polarization function (d), introducing a set of d functions on heavy atoms.[30] A polarizable continuum model (PCM)[31] was employed as a solvation model within the default SCRF methods to account for the aqueous solvation effect, using water as the solvent. These functional parameters were specified in the route section to calculate the low-energy molecular structure, oscillation frequency, and IR intensity. All DFT calculations were performed using Gaussian 09 software,[32] and the results were visualized using GaussView.[32]

2.3. Quantifying Precipitation Rates from Solution Conductivity. $CaCO_3$ precipitation rates were assessed by monitoring the conductivity over time in supersaturated growth solutions (50 mM $CaCl_2$, 50 mM $NaHCO_3$) containing 10 mM of a selected bisphosphonate molecule. Stock solutions were prepared by dissolving sodium bicarbonate ($NaHCO_3$) (Certified ACS, Fisher Chemical) or calcium chloride dihydrate ($CaCl_2{\cdot}2H_2O$) (Certified ACS, Fisher Chemical) in deionized water (Milli-Q, >18.2 MΩ·cm). Bisphosphonate stock solutions were created by dissolving the synthesized molecules, as outlined in Section 2.1, in deionized

Table 1. Summary of Experiments Conducted and pH Measured Immediately Following the Addition of $CaCl_2{\cdot}2H_2O$ to $NaHCO_3$ with and without Bisphosphonates

Experiment Type	$CaCl_2{\cdot}2H_2O$ (mM)	$NaHCO_3$ (mM)	Additive (mM)	Additive Type	T (°C)	Time (h)	pH
In Situ AFM	2	2	0	-	25	0.5	8.16
	2	2	2	C3-COOH	25	2.0	3.34
	2	2	2	C3-OH	25	2.0	3.36
	2	2	2	C7-COOH	25	0.75	3.22
	2	2	2	C7-OH	25	0.75	3.20
	2	2	2	C11-COOH	25	1.0	3.24
	2	2	2	C11-OH	25	1.5	3.29
	2	2	2	C11-CH3	25	3	n.m.[a]
Precipitation Rate (Conductivity)	50	50	0	-	25	240	n.m.
	50	50	10	C3-COOH	25	240	n.m.
	50	50	10	C3 OH	25	240	n.m.
	50	50	10	C7-COOH	25	240	n.m.
	50	50	10	C7-OH	25	240	n.m.
	50	50	10	C11-COOH	25	240	n.m.
	50	50	10	C11-OH	25	240	n.m.
	50	50	10	C11-CH3	25	240	n.m.
Precipitate Characterization (FTIR, TGA)	80	80	0	-	25	240	n.m.
	80	80	10	C3-COOH	25	240	n.m.
	80	80	10	C3-OH	25	240	n.m.
	80	80	10	C7-COOH	25	240	n.m.
	80	80	10	C7-OH	25	240	n.m.
	80	80	10	C11-COOH	25	240	n.m.
	80	80	10	C11-OH	25	240	n.m.
	80	80	10	C11-CH3	25	240	n.m.

[a] n.m. = not measured because of the limited amounts of bisphosphonates synthesized.

water for at least 30 min. $NaHCO_3$, $CaCl_2{\cdot}2H_2O$, and bisphosphonate stock solutions were prepared in separate high-density polyethylene bottles. Subsequently, growth solutions were formulated by combining the concentrated stock solutions in the following sequence: (1) $NaHCO_3$, (2) bisphosphonate molecule, (3) deionized water, and (4) $CaCl_2{\cdot}2H_2O$. The conductivity of the solution was measured immediately after mixing and then every 30 s for up to 4 h, while stirring at 400 rpm using a magnetic stirrer. Conductivity measurements at 25 °C were conducted using an Orion Versa Star Pro meter (Thermo Fisher Scientific) equipped with a built-in ATC conductivity probe, applying linear temperature compensation. The measured conductivity was translated to the Ca^{2+} concentration using a four-point calibration curve. Calibration solutions were made from the same stock solutions with concentrations of 0 mM (deionized water only), 10 mM, 40 mM, and 80 mM for both $NaHCO_3$ and $CaCl_2{\cdot}2H_2O$ and 10 mM bisphosphonate additive (refer to Figure S45). The initial conductivity of each growth solution was recorded immediately upon mixing for each calibration curve. Due to rapid precipitation initially, the actual initial conductivity could not be directly measured; hence, each concentration curve was adjusted by adding a predetermined offset value (as detailed in Figure S46 and Table S2).

2.4. Characterization of Precipitates. After 10 days, the precipitates obtained from the conductivity measurements were separated from the supernatant through centrifugation at 3000 rpm using a Horizon 24 Flex centrifuge (Drucker Diagnostics). An extrapolation of the uncorrected conductivity curves suggests that equilibrium is achieved within approximately 10 days for most samples, maximizing the amount of precipitates for subsequent analysis. The separated precipitates were then dried in a vacuum desiccator for 11 to 31 days before being stored at room temperature. The extended drying time is necessary because of the high water content of the precipitates. Characterization of the precipitates was conducted using Fourier-transform infrared spectroscopy (FTIR) on a Nicolet iS50 spectrometer (Thermo Fisher Scientific), employing attenuated total reflectance over a scan range of 4000−525 cm^{-1}. Additionally, the precipitates were characterized using thermogravimetric analysis (TGA) on a Q600 SDT (TA Instruments), with a heating rate of 15 °C/min from ambient temperature up to 1000 °C under an ultrahigh purity (UHP) N_2 gas flow of 20 mL/min. Selected samples were subjected to repeat TGA analysis to assess changes in dehydration over time. The mass distribution of $CaCO_3$ polymorphs was determined from differential mass data using Igor Pro software.[33] Scanning electron microscopy (SEM) and energy dispersive spectroscopy (EDS) analyses were performed on chosen samples using a Hitachi S-3000N Variable Pressure SEM, set to a working distance of 15 mm and an accelerating voltage of 25 kV. Prior to SEM imaging, powder samples were finely ground and coated with Au/Pt for 2 min using a Hummer VI sputtering system.

2.5. In Situ Atomic Force Microscopy. Stock solutions were prepared using a method similar to that described in Section 2.3. The bisphosphonate-containing solution was mixed with a concentrated (50 mM) $NaHCO_3$ solution, and the mixture was diluted with deionized water to the desired concentrations (4 mM). Calcite substrates were created by cleaving a single crystal calcite (Iceland Spar, Brazil) into plates approximately 1 cm in length, 1 cm in width, and 1 mm in height by using a razor blade. Freshly cleaved calcite substrates were affixed to magnetic discs by using double-sided carbon tape to expose the calcite (104) surface. This surface was then cleaned with a brief blast of UHP N_2 gas to remove dust from the cleaving process.

In situ imaging was carried out with a Cypher ES atomic force microscope (AFM) (Oxford Instruments Asylum Research) at a constant temperature of 25 °C. A monolithic silicon probe, coated with gold on the detector side (spring constant, $k = 3$ N/m, resonance frequency, $f = 75$ kHz in air and $f \approx 31$ kHz in solution), was mounted in a sealed fluid cell equipped with inlet and outlet ports for solution infusion and withdrawal. This configuration ensures that the reaction solution comes into contact only with the AFM probe, stainless steel probe clamp, fused silica, PEEK O-ring, and calcite substrate.

The calcite substrate was equilibrated with deionized water for at least 1 h or until no further dissolution was observed, whichever occurred later. A micro-T connector, attached to the fluid cell inlet, was used to instantly mix (<3 s) 4 mM $CaCl_2$ and either 4 mM

Table 2. Speciation Calculations for Solutions without Additives: (*italic*) As-Prepared and (bold) after Equilibration with Atmospheric CO_2

$CaCl_2$ (mM)	$NaHCO_3$ (mM)	pH	pCO_2 (log atm)	SI Calcite	SI Aragonite	$\{Ca^{2+}\}$ (M)	$\{HCO_3^-\}$ (M)	$\{CO_3^{2-}\}$ (M)
2	*2*	*8.02*	*−2.96*	*0.57*	*0.42*	1.94×10^{-3}	1.89×10^{-3}	1.16×10^{-5}
2	**2**	**8.44**	**−3.40**	**0.95**	**0.81**	1.91×10^{-3}	1.78×10^{-3}	2.87×10^{-5}
50	*50*	*7.57*	*−1.28*	*2.35*	*2.21*	4.16×10^{-2}	3.86×10^{-2}	1.57×10^{-4}
50	**50**	**9.18**	**−3.40**	**3.37**	**3.22**	3.21×10^{-2}	1.19×10^{-2}	1.87×10^{-3}
80	*80*	*7.50*	*−1.06*	*2.58*	*2.43*	6.35×10^{-2}	5.79×10^{-2}	2.29×10^{-4}
80	**80**	**9.24**	**−3.40**	**3.61**	**3.47**	4.87×10^{-2}	1.41×10^{-2}	2.86×10^{-3}

$NaHCO_3$ or a bisphosphonate-containing solution of 4 mM $NaHCO_3$, just before introducing it to the calcite substrate. This approach minimizes the homogeneous precipitation and settling of $CaCO_3$ before the AFM analysis.

A syringe pump introduced the growth solution (2 mM $NaHCO_3$, 2 mM $CaCl_2$, and 2 mM bisphosphonates) into the fluid cell. Before imaging in the growth solutions, approximately 0.3 mL of the residual solution was withdrawn. Images were acquired in AC (tapping) mode at a scan rate of 4.88 Hz, covering areas between 4 and 64 μm^2. Each image acquisition was collected over 1 min and 45 s. Image postprocessing was performed using Gwyddion 2.58[34] and was limited to first-order background subtraction for planar slope correction. Separately, solutions were prepared for pH measurements, consisting of 50 mM of each stock solution ($NaHCO_3$, $CaCl_2$, and bisphosphonate) and 2 mM of growth solution. pH values were measured immediately (within 10 s) after mixing the stock solutions.

3. RESULTS AND DISCUSSION

3.1. Solution Chemistry. The details of the experiments performed are listed in Table 1. Geochemical modeling of the growth solution without additives was carried out using PHREEQC[35] with the LLNL database (Table 2). The simulations indicate that the solutions are supersaturated with respect to calcite and aragonite, featuring a pCO_2 higher than the ambient atmospheric level, which allows potential degassing that could increase the pH and the CO_3^{2-} activity. The actual measured pH values of the growth solutions aligned with the modeled predictions, indicating that immediate significant CO_2 degassing did not occur. Given that the bisphosphonate solutions are acidic (as shown in Table 3), the addition of $NaHCO_3$ leads to rapid deprotonation of the bisphosphonates (refer to pK_a values in Section 3.2) before the introduction of Ca^{2+}. The concentrations of dissolved compounds were chosen to match the temporal and spatial resolution required for the specific measurements and to reflect typical conditions found in environments relevant to this study, such as cementitious pore solutions and biological mineralization processes.[36] It is noteworthy that the inherently acidic nature of bisphosphonate molecules resulted in a growth solution with pH of less than approximately 3.4 (Table 1), whereas previous studies in similar contexts have been conducted at pH levels ranging from 6 to 10.[17,37−39] As further discussed, bisphosphonates, regardless of functional group and chain length, stabilize CO_3^{2-} anions and promote $CaCO_3$ formation even under acidic conditions.

Table 3. Measured pH Values of Representative Stock Solutions Used in This Study

Solution	pH
50 mM $NaHCO_3$	8.39
50 mM $CaCl_2 \cdot H_2O$	5.69
50 mM C3-COOH	1.63
50 mM C3-OH	1.63
50 mM C7-COOH	1.59
50 mM C7-OH	1.51
50 mM C11-COOH	1.60
50 mM C11-OH	1.76

3.2. Characterization of Bisphosphonate Molecules. *3.2.1. pK_a and Lipophilicity.* The synthesized bisphosphonate molecules in this study are depicted in Figure 2. These molecules consist of a bisphosphonate group linked to a functional group that is either negatively charged (−COOH) or neutrally charged (−OH), with the two groups separated by a chain of three, seven, or eleven carbons. Additionally, the study includes a bisphosphonate molecule with a nonpolar, uncharged functional group (CH_3). Bisphosphonate moieties contain four acidic protons, and their acid dissociation constants (pK_a) are documented in the literature (refer to Figure 3).[40] The pK_a values significantly affect the molecules' physical properties, such as solubility, lipophilicity, and binding capacity.[41,42] Various semiempirical methods are available for predicting these properties. For example, Chemaxon[43] has shown logical trends aligned with structural differences that generally concur with previously published values (see Table 4

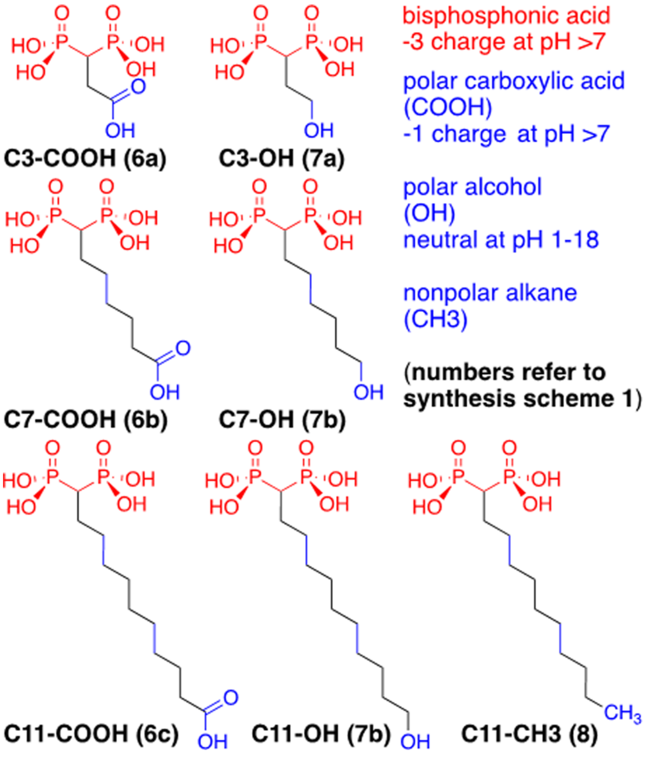

Figure 2. Diagram of bisphosphonate molecules examined, highlighting side chain lengths (black) and functional groups (in blue).

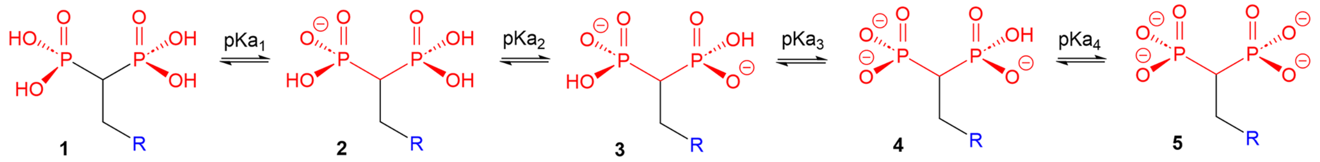

Figure 3. Protonation states of bisphosphonate molecules (chain length not specified in this figure).

Table 4. Estimated pK_a and Lipophilicity (logP) Values for Bisphosphonates Using Chemaxon[43]

Molecule	pK_{a1}	pK_{a2}	pK_{a3}	pK_{a4}	pK_{a5}	Lipophilicity (logP)
C3-COOH	1.20	1.96	4.54	7.99	8.7	−3.03
C3-OH	1.21	1.97	7.87	8.58	15.99	−3.25
C7-COOH	1.21	1.97	6.55	7.98	8.68	−1.79
C7-OH	1.21	1.97	7.87	8.58	−1.99	−2.00
C11-COOH	1.21	1.97	4.95	7.87	8.58	−2.00
C11-OH	1.21	1.97	7.87	8.58	−1.99	−0.42
C11-CH3	1.21	1.97	7.87	8.58	N/A	1.03

and Figure 3), except for the fourth pK_{a4} value. This discrepancy may arise because Chemaxon's predictions for bases are not as accurate as for acids.[44] Importantly, at the experimental pH of approximately 3.4, the species predominantly exists in a doubly deprotonated form (refer to Species 3 in Figure 3), indicating that under the experimental conditions, the bisphosphonate groups of all molecules are likely to bear a negative charge, suggesting a strong affinity for positively charged ions in the growth solutions. Furthermore, the negative lipophilicity (logP) values suggest that these molecules are more soluble in aqueous environments than in organic solvents (Table 4).

3.2.2. Binding Energies. Based on the pK_a values from the literature[40] and the calculations presented in Table 4, species 4 (depicted in Figure 3) is presumed to be the prevalent species formed upon the addition of the $NaHCO_3$ solution (before the introduction of the $CaCl_2 \cdot 2H_2O$ solution). Consequently, the overall charge state is −4 for bisphosphonates bearing a COOH group and −3 for those with OH^- and CH_3 when exposed to basic $NaHCO_3$ solutions (as illustrated in Figure S47). Computational analyses were conducted by positioning the Ca^{2+} ion at specific sites around C11-COOH and C3-COOH molecules to determine the minimum binding energy (expressed in Hartree, shown in Figure 4). For molecules with an 11-carbon chain, the binding of Ca^{2+} to two oxygen atoms in the phosphonate groups is preferred (as demonstrated in Structures 1−3 in Figure 4). These changes in free energy are consistent with studies on other methylenebisphosphonates.[45,46] The binding energy for this preferred configuration remains relatively consistent across different functional groups (as seen in Structures 1, 4, and 5 in Figure 4). Notably, the smaller C3-COOH molecule exhibits a different Ca^{2+} chelation pattern (Structure 6 in Figure 4), likely forming a cyclic

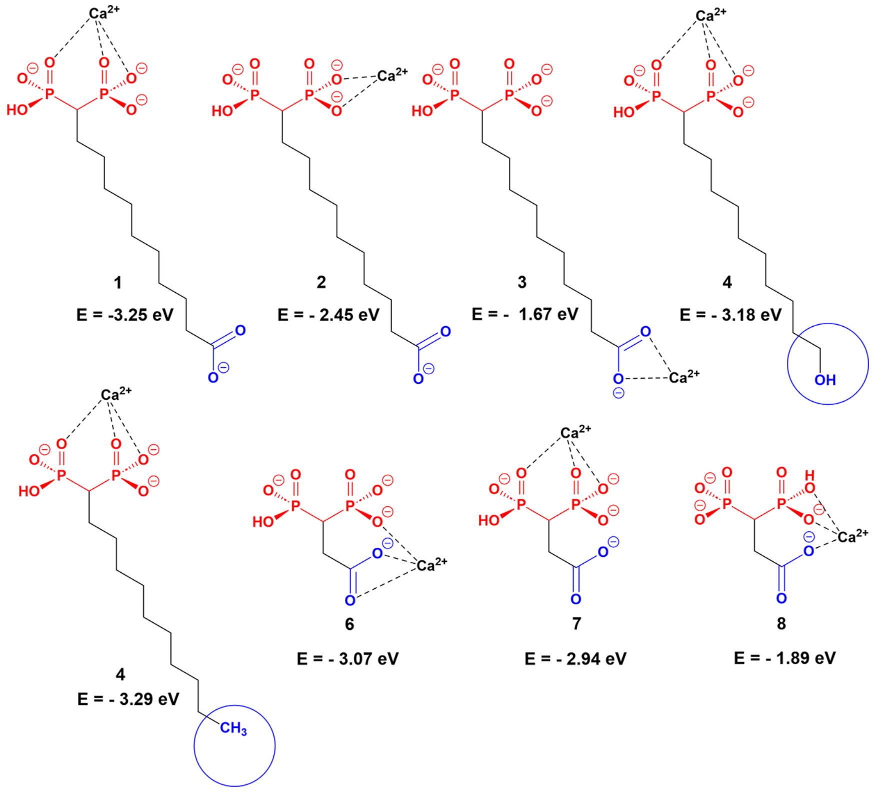

Figure 4. Structural interactions and binding energies of Ca^{2+} with different binding modes for (**1**−**3**) C11-COOH, (**4**) C11-OH, (**5**) C11-CH3, and (**6**−**8**) C3-COOH, demonstrating the impact of alkyl chain length and functional group.

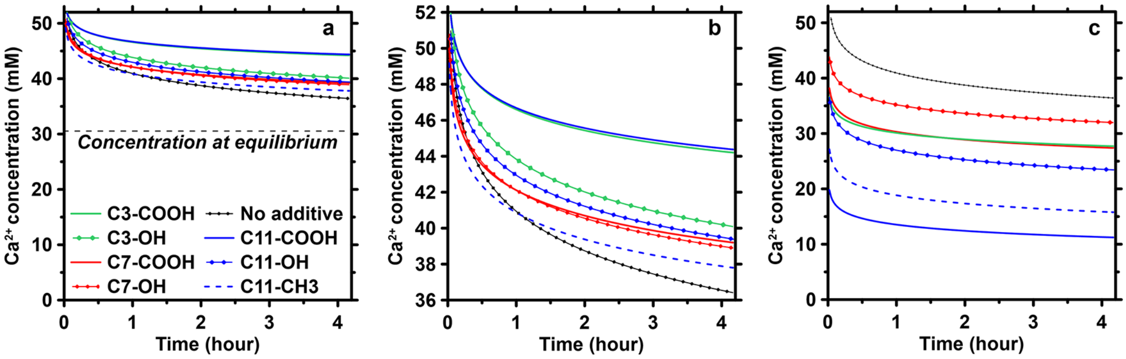

Figure 5. Variation of Ca^{2+} concentration over time, inferred from solution conductivity, across growth solutions of varying bisphosphonate additives: (a) Original curves highlighting the secondary (slower) precipitation phase. The equilibrium Ca^{2+} concentration determined through PHREEQC calculations is shown. (b) Detailed examination of (a). (c) Adjusted curves illustrating the precipitate rate and extent during both rapid and slow phases (Note: No adjusted curve is available for C3-OH).

structure due to the lower entropic barriers associated with its shorter side chain.[47]

3.3. Solution Conductivity Reveals Accelerated Calcium Carbonate Precipitation. In the conductivity experiments (Table 1), mixing Ca- and bisphosphonate-containing $NaHCO_3$ stock solutions immediately resulted in visible white precipitates. This initial rapid precipitation phase is succeeded by a gradual decrease in conductivity and Ca^{2+} concentration, suggesting a secondary, slower precipitation phase. Without adjustment for the rapid initial precipitation, the conductivity curves (Figure 5a) revealed that solutions with OH-bearing bisphosphonates had lower final Ca^{2+} concentrations compared to those with COOH-bearing bisphosphonates, indicating that negatively charged molecules not only promote faster initial precipitation but also result in lower Ca^{2+} availability for the subsequent precipitation phase (Figure 5b).

We estimate the extent of initial precipitation using mass balance, assuming the precipitates were purely $CaCO_3$ (details in Section 2 of the Supporting Information, Table S2, and Figure S46). However, incorporating bisphosphonates into the precipitates leads to an underestimation of Ca^{2+} concentrations by 6.92−33.14 mM. After correcting for the precipitate mass collected at the experiment's conclusion (except for the C3-OH sample, which lacked sufficient mass for correction), the data indicated that bisphosphonates enhanced the precipitation rate and extent, especially in the initial phase, when compared to the control group without additives (as illustrated in Figure 5b). Particularly, the fastest initial precipitation rates were observed with 11-carbon bisphosphonates (Figure 5c). Within molecules of identical chain lengths, those with the negatively charged COOH group induced faster initial precipitation than those with the neutral OH group (Figure 5c). The precipitation rates stabilized across all experiments after 1 h of reaction. The similar effects of C7-COOH and C3-COOH on the precipitation rate highlight a critical chain length for the effective acceleration of $CaCO_3$ precipitation (Figure 5c). Overall, the presence of additives reduced the ultimate Ca^{2+} concentration compared to the control, implying that additives decrease the solubility of the precipitating carbonate phase, a topic to be elaborated on further.

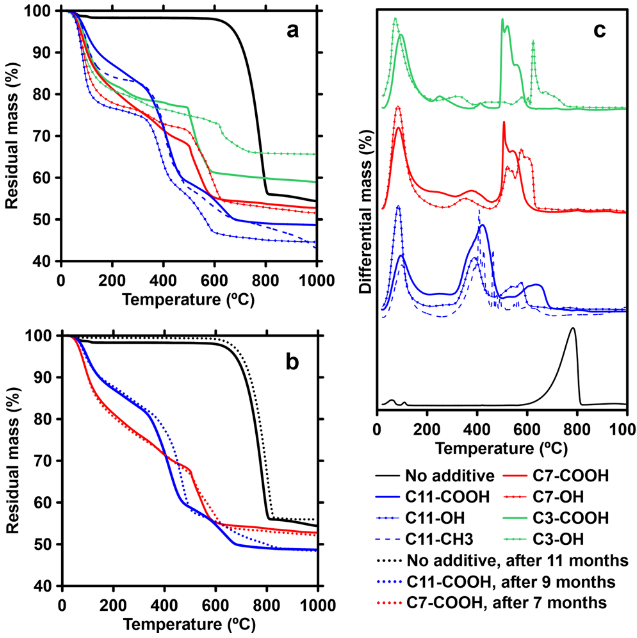

Figure 6. Thermogravimetric analysis of precipitates described in Section 3.3, showing (a) the residual mass due to dehydration and decarbonation, (b) stability of selected samples upon remeasurement after seven to 11 months of ambient storage, and (c) differential mass across temperature ranges, highlighting the influence of different bisphosphonates on the formation of $CaCO_3$ polymorphs.

3.4. Influence of Molecular Chain Length and Functional Group on Polymorph Selection. We performed TGA on the precipitates produced in Section 3.3 to identify the specific $CaCO_3$ polymorphs present (Figures 6 and 7). The thermogravimetric data revealed decomposition phases over temperature ranges of 20−160 °C due to water evaporation and two distinct phases at 270−470 °C and 570−930 °C attributed to the decarbonation of $CaCO_3$ (Figure 6a,c).[3,48−52] Generally, a higher degree of crystallinity corresponds to higher decomposition temperatures, for example, ACC, vaterite, and calcite decompose at 550−650 °C, 650−720 °C, and approximately 790 °C.[3,51] The control sample exhibited two transitions: the initial one associated with dehydration and the second at 800 °C corresponding to the decomposition of calcite (Figure 6a).[51] The dehydration peak indicates the possible presence of ACC in the control sample.

In contrast, in samples with bisphosphonate additives, ACC (decomposing between 300 and 490 °C) and presumably vaterite (490−760 °C) were preferentially formed, irrespective of the functional group present (Figure 6a). Notably, ACC formation was particularly favored with 11-carbon bisphosph-

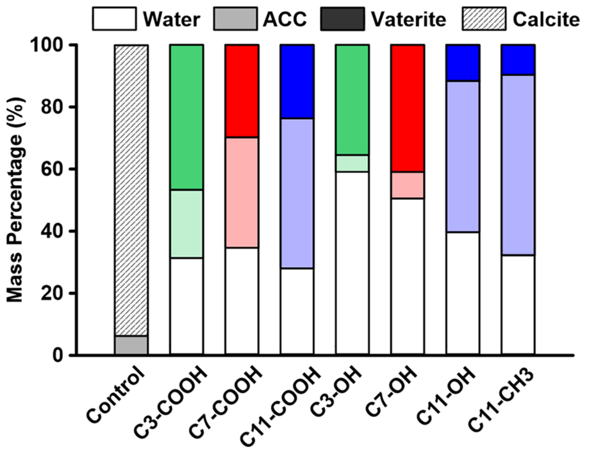

Figure 7. Phase assemblage (by mass) was obtained from differential mass loss.

onates, whereas vaterite formation was more common with the 3- and 7-carbon chains (Figure 6c). The mass loss for the samples with 7- and 11-carbon bisphosphonates exceeded that of the control, suggesting that the bisphosphonate molecules themselves contributed to the mass loss . This finding is consistent with results from FTIR and SEM-EDS analyses, which indicate [P]:[Ca] molar ratios of 0.63 and 0.82 (mol/mol) for samples synthesized with C7-OH and C11-OH (Table S3).

Assuming that the precipitates are solely composed of pure $CaCO_3$ may lead to an overestimation of the ACC mass percentage. This overestimation occurs because the decomposition temperatures for the alkyl chain bisphosphonates (up to 350 °C)[53] fall within the ACC decomposition range, and the molar masses of bisphosphonates are significantly higher than that of $CaCO_3$. If bisphosphonates decompose at higher temperatures, it could also increase the estimated mass percent of vaterite.

Repeated TGA measurements confirmed that the precipitated ACC and vaterite remain stable for over 7 months when stored in ambient conditions (Figure 6b). This stability suggests that the precipitates adopt a hydrate form, which has been shown to enhance the stability of both ACC and vaterite in their anhydrous states.[10,54]

The infrared absorbance spectrum of ground single-crystal calcite shows distinct characteristic peaks at 713 (v_4), 870 (v_2), and 1390 (v_3) cm^{-1} and a minor peak at 1085 cm^{-1} (v_1), as depicted in Figure 8a,b.[3,55] Additionally, the control sample (without additives) displayed a broad peak around 3400 cm^{-1} and a smaller peak at 1630 cm^{-1}, indicative of ACC, as also seen in Figure 8a,b.[3,55] Thermogravimetric analysis further supports this, with a transition noted for water removal from room temperature to 120 °C in the control sample (Figure 6c). Since the sample was dry at the time of TGA, the detected water molecules must be chemically bounded, which reinforces the presence of ACC in the control sample.

The inclusion of bisphosphonate molecules in the growth solutions modified the $CaCO_3$ structure, as shown in Figure 8. This modification is evidenced by new peaks at 2845 and 2925 cm^{-1} (attributed to sp^3 CH bonds) and 912 and 1133 cm^{-1} (corresponding to phosphonate groups) across all samples containing bisphosphonates (Figure 8b). Notably, changes in the P═O and P−O bond strengths, with a shift of the P═O peak from 1133 to 1058 cm^{-1} and the P−O peak from 912 to 952 cm^{-1}, suggest that Ca^{2+} ions preferentially bind to the oxygen of the P═O group rather than the negatively charged oxygen of the P−O group. This binding leads to electron density withdrawal from the P═O double bond and electron donation to the P−O single bond, weakening the P═O bond and strengthening the P−O bond, thereby shifting their respective peaks (Model A in Figure 8c). These findings are

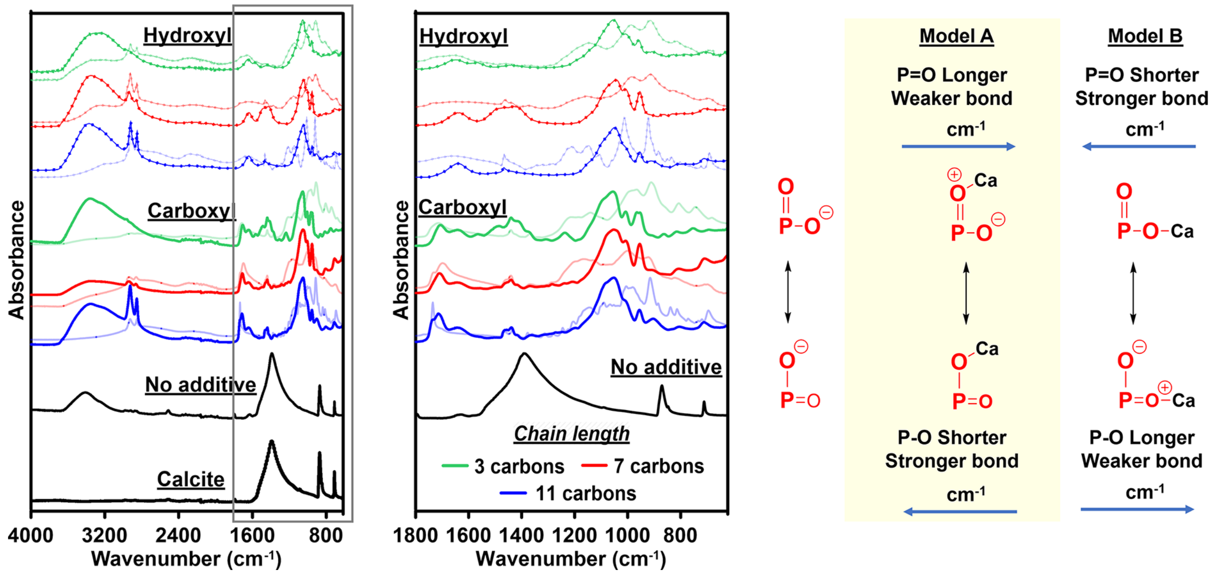

Figure 8. Infrared absorbance spectra of precipitates from the conductivity experiments. (a), Overall spectra; (b) Zoomed-in view of (a) for detailed analysis. (c) Illustration of the phosphonate group's potential binding modes with Ca^{2+} ions. The leftmost panel displays two resonance structures of the phosphonate group. On the right, two possible interactions of Ca^{2+} with the phosphonate group are depicted. Starting from the top, Ca^{2+} may bond with the oxygen in P═O (Model A) or with negatively charged oxygen (O^-) in P−O (Model B). FTIR results suggest a preference for Ca^{2+} to bind via Model A, leading to a weakened P═O bond and a strengthened P−O bond. Conversely, Model B would have the opposite effect and is considered less favorable due to charge separation.

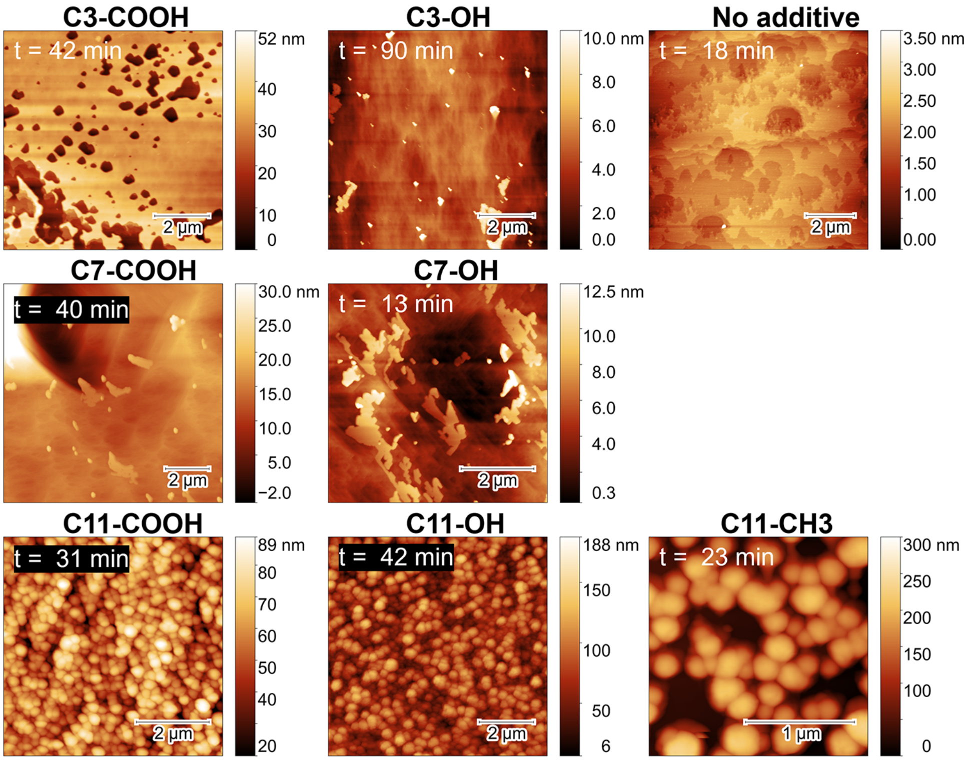

Figure 9. In situ AFM height images of calcite surfaces exposed to various experimental solutions with reaction times noted for each respective image.

consistent with DFT modeling results and the high affinity of bisphosphonate groups for Ca^{2+} ions.[26,56]

In samples with negatively charged bisphosphonates, the C═O peak (1670 to 1757 cm^{-1}) remains unchanged, implying that the carboxyl group is not the primary site for Ca^{2+} binding (Figure 8b). The introduction of bisphosphonates also led to the disappearance or shift of calcite peaks, hinting at the formation of ACC and possibly vaterite. Evidence for ACC's persistence includes the intensity reduction and broadening of the v_4 band, alteration of the v_3 band into a double peak that is shifted by 40 cm^{-1} to a higher wavenumber, and the emergence of water peaks. No distinct vaterite peaks were observed except for a possible peak at 744 cm^{-1} in the C3-COOH sample, which might also be attributable to the bisphosphonate molecule itself (Figure 8b). Moreover, X-ray diffraction (XRD) analysis of the C11-COOH sample revealed the absence of any Bragg peaks, indicating the formation of ACC (Section 5 in Supporting Information, Figure S48).[57]

3.5. Influence of Molecular Chain Length on Morphology Selection.

Morphological analysis offers insights into how bisphosphonates are incorporated into precipitates. In situ AFM imaging revealed that, in the absence of additives, $CaCO_3$ growth on the calcite (104) surface progresses through the advance of existing monolayer calcite steps (Figure 9). Introducing bisphosphonate-containing growth solutions led to the rapid dissolution of calcite through etch pit formation, suggesting that these solutions are undersaturated with respect to calcite. This undersaturation likely results from Ca^{2+} complexation with bisphosphonates, consistent with our FTIR observations.[38,58]

With 3-carbon and 7-carbon bisphosphonates, we observed rapid nucleation and expansion of flat, two-dimensional (2D) islands, with heights ranging from 10−40 nm or 2−10 nm (Figure 9). Corresponding height profiles are shown in Figure S49. Notably, in the sample with C3-COOH bisphosphonates, the islands coalesced to form a nearly continuous film spanning several square micrometers (Figure 9). The polygonal shapes of even the smaller 2D islands suggest epitaxial growth influenced by the substrate (Figure 9).

In contrast, the introduction of 11-carbon bisphosphonates led to the development of semispherical, three-dimensional (3D) islands, regardless of the functional group present (Figure 9). The average grain diameters for samples with COOH, OH, and nonfunctionalized bisphosphonates were about 350, 420, and 310 nm, larger than previously observed ACC sizes.[17,57−59] The tendency of longer hydrophobic alkyl chains to form micelles suggests that these structures could serve as nucleation sites for ACC. The critical micelle concentration, found to be 2.12 mM (detailed in Section 6 of the Supporting Information, Figure S50), is similar to the 2 mM concentration used in our morphological studies. Hence, micelle formation can partially account for the observed semispherical morphology.

3.6. Mechanism of $CaCO_3$ Precipitation in the Presence of Bisphosphonates and Implications for Construction Applications.

The structural transformations observed in precipitates formed with bisphosphonate additives suggest strong ionic interactions with Ca^{2+} ions during both nucleation and growth. Importantly, Ca^{2+} ions show a preference for binding with the bisphosphonate group, leading to the stabilization of ACC particles without inhibiting $CaCO_3$ formation, regardless of the bisphosphonate's functional group or chain length (Figure 6a,c).[60,61]

The binding of amino acids to Ca^{2+} is highly dependent on the local environment, with side chains or neighboring amino

https://doi.org/10.1021/acsami.4c04218
ACS Appl. Mater. Interfaces 2024, 16, 30567−30579

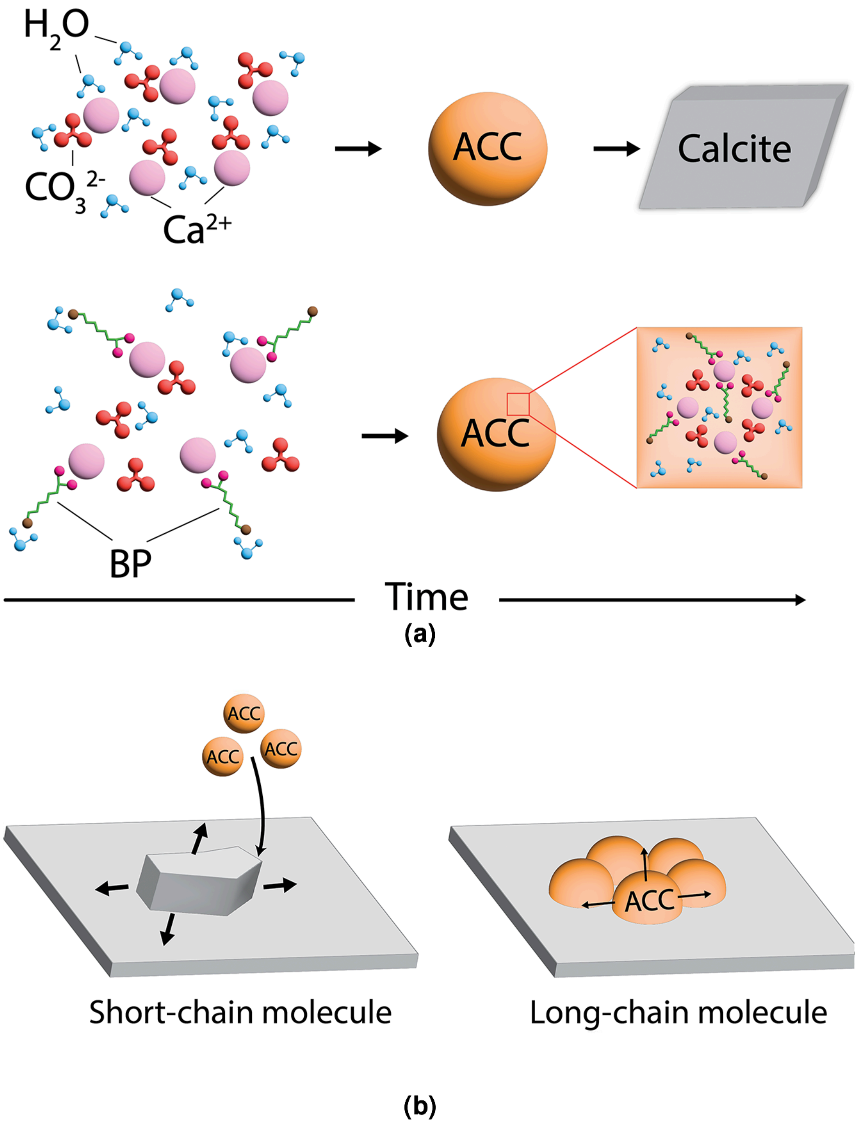

(a)

(b)

Figure 10. Illustrated mechanism of metastable ACC stabilization by bisphosphonates during (a) homogeneous nucleation and (b) heterogeneous nucleation. For homogeneous nucleation, ACC that forms in the absence of additives may transform to calcite, whereas with bisphosphonate additives, Ca^{2+} ion complexation with bisphosphonate stabilizes ACC by reducing its solubility and preventing the nucleation of calcite. During heterogeneous nucleation, in both the absence and presence of additives, the formation process of either calcite or a combination of ACC and vaterite adheres to nonclassical crystal growth theories, which involve ACC precursors attaching to the calcite surface as observed in AFM studies. The addition of bisphosphonates (BP) stabilizes ACC and vaterite through surface modifications, hindering their attachment to calcite surfaces and preventing their transformation into calcite.

acids in proteins affecting Ca^{2+} interactions.[25] The methylene bisphosphonates used here bind calcium strongly, and variations in side-chain effects can fine-tune $CaCO_3$ formation without significantly altering the bisphosphonate-calcium interaction dynamics.[62]

Considering the chain length effects and bisphosphonate-ion interactions in the growth solution, we propose a mechanism for ACC formation and stabilization in the presence of bisphosphonate, as detailed in Figure 10. We differentiate between homogeneous nucleation (characterization samples) and heterogeneous nucleation (AFM experiments).

In homogeneous nucleation, ACC typically forms as a precursor and undergoes a dissolution-reprecipitation process, eventually transitioning to more stable phases such as calcite, aragonite, or vaterite. Previous studies have reported this mechanism for ACC to calcite conversion.[9,17,24,63,64] Bisphosphonates may slow down the dissolution of ACC, the nucleation and growth of crystalline phases, or both. TGA results confirming both ACC and vaterite formation suggest that bisphosphonates stabilize ACC by reducing its solubility while selectively inhibiting calcite nucleation. It has been proposed that smaller ACC-poly(acrylic acid) aggregates stabilize ACC through strong and random Ca and water interactions, leading to long-lasting ACC precipitates.[57] Similarly, bisphosphonate additives form specific complexes with Ca^{2+}, acting as nucleation sites for stable ACC formation. The timing of bisphosphonate-calcium complexation may influence ACC stability; short complexation times in poly(acrylic acid) have been shown to increase ACC stability.[57] Likewise, this rapid complexation likely contributes to the stability observed for ACC in this study. Additionally, bisphosphonates with longer chains demonstrate stronger hydrophobic effects and intramolecular interactions, which tend to precipitate ACC more rapidly. At the molecular level,

https://doi.org/10.1021/acsami.4c04218
ACS Appl. Mater. Interfaces 2024, 16, 30567−30579

organic molecules can expand the free volume within ACC,[64] thereby lowering the energy barrier to crystallization. When this concept is applied to bisphosphonates, they likely encapsulate more water within the ACC structure, maintaining it in a hydrated form, which is more stable than its anhydrous counterpart.

The formation of vaterite was notably higher with the addition of 3-carbon bisphosphonates, irrespective of the functional group. This phenomenon can be explained by the reduced energy barrier for the structural reorganization of ACC facilitated by the incorporation of shorter-chain bisphosphonates. This lower barrier is crucial for ACC's transformation into vaterite.[9,57,64] This explains the increased formation of vaterite, indicating that the shorter hydrophobic chain length plays a significant role in ACC's structural reorganization and subsequent vaterite formation.

For heterogeneous nucleation, a nonclassical crystal growth mechanism through an ACC precursor has been proposed.[63] According to this model, calcite growth occurs via the attachment and organization of ACC particles into 2D islands. This process mirrors observations in samples with 3- and 7-carbon bisphosphonates. In the absence of additives, ACC attaches to the existing calcite substrate, facilitating monolayer growth and thereby maintaining crystallographic compatibility between the new layers and the calcite substrate. The addition of bisphosphonates, however, distorts the ACC and to some extent vaterite structures, promoting the epitaxial growth of both flat 2D islands and semispherical 3D islands on the calcite substrate. The lattice misfit likely increases with the chain length, as indicated by the distinct morphologies observed.

The emergence of semispherical 3D morphologies with the introduction of 11 carbon-chained bisphosphonates can be attributed to the formation of stable ACC with a more distorted structure. Rather than forming flat islands, ACC particles deposited on the calcite substrate and grew outward. This growth pattern follows the Volmer–Weber epitaxial growth model.[65] Conversely, the layer-by-layer growth of flat 2D islands, seen with the addition of 3 and 7 carbon-chained bisphosphonates, follows the Frank-van der Merwe model.[66] The thickness of these newly formed layers (ranging from 2 to 30 nm) significantly exceeds that of a single calcite layer (~3 Å), suggesting that the two remain structurally distinct, implying a balance in the lattice misfit that explains the observed morphology.

Considering the findings from homogeneous nucleation studies, these newly formed 2D islands are likely orthorhombic vaterite growing atop a rhombohedral calcite (104) surface.[67,68] The interaction of bisphosphonates with the calcite substrate, leading to its dissolution, not only supports the hypothesis that bisphosphonates inhibit calcite nucleation in homogeneous nucleation scenarios but also implies their role in promoting calcite dissolution.

Several studies utilizing organic additives as admixtures to produce ACC and vaterite have observed increases in the compressive strength and flexural strength. These increases in strength are attributed to smaller grain sizes and higher surface areas of metastable $CaCO_3$, which increase reactivity.[3,69,70] Our study shows that bisphosphonates influence not only the polymorph and morphology but also the rate of $CaCO_3$ precipitation and that the specific effects are contingent upon chain length and functional group. These insights enable the design of novel molecules that facilitate the formation of the desired $CaCO_3$ phases.

4. CONCLUSIONS

We successfully synthesized unique bisphosphonate molecules with a range of chain lengths and functional groups, enabling a detailed examination of their impact on calcium carbonate precipitation. Our findings indicate that bisphosphonates with various functional groups can promote the formation of ACC and vaterite, which remains stable for at least seven months. Molecules with longer chains tended to increase the proportion of ACC compared to vaterite and influenced the precipitate morphology to transition from 2D to 3D islands. The strong binding of Ca^{2+} to the bisphosphonate functional groups results in the incorporation of these molecules into the precipitates, leading to notable alterations in their chemical structure and morphology.

This research highlights the critical role of the interactions of Ca^{2+} with bisphosphonate groups in directing both polymorph selection and morphological outcomes during $CaCO_3$ precipitation. It appears that the chain length of amphiphilic bisphosphonates, rather than their net charge, predominantly influences these processes. Intriguingly, our results suggest the presence of a specific chain length threshold for bisphosphonates that dictates the formation of certain $CaCO_3$ polymorphs and morphologies. These insights could prove valuable in tailoring the microstructure and properties for construction applications, particularly in the development of carbonate-based binders for cementation processes.

■ ASSOCIATED CONTENT

Supporting Information

The Supporting Information is available free of charge at https://pubs.acs.org/doi/10.1021/acsami.4c04218.

Synthesis and NMR data (^1H, $^{13}C\{^1H\}$, and ^{31}P) for bisphosphonate molecules, conductivity calibration curve and method for correcting the calibration curve, deprotonation states of bisphosphonate under the experimental pH values, XRD pattern of calcite and sample with C11-COOH, height profiles of 2D islands on calcite, critical micelle concentration determination, and EDS data for C, O, P, and Ca in the precipitate (PDF)

■ AUTHOR INFORMATION

Corresponding Authors

Erika La Plante – *Department of Materials Science and Engineering, University of California, Davis, Davis, California 95616, United States;* orcid.org/0000-0002-5273-9523; Email: eclaplante@ucdavis.edu

Frank W. Foss, Jr. – *Department of Chemistry and Biochemistry, University of Texas at Arlington, Arlington, Texas 76019, United States;* orcid.org/0000-0003-1940-6580; Email: ffoss@uta.edu

Authors

Trinh Thao My Nguyen – *Department of Materials Science and Engineering, University of California, Davis, Davis, California 95616, United States*

Shan Hazoor – *Department of Chemistry and Biochemistry, University of Texas at Arlington, Arlington, Texas 76019, United States*

Thanh Vuong – *Department of Chemistry and Biochemistry, University of Texas at Arlington, Arlington, Texas 76019, United States*

LeMaur Kydd − *Department of Mathematics, University of Texas at Arlington, Arlington, Texas 76019, United States*

Ian Shortt − *Department of Materials Science and Engineering, University of California, Davis, Davis, California 95616, United States; Department of Materials Science and Engineering, University of Texas at Arlington, Arlington, Texas 76019, United States*

Complete contact information is available at:
https://pubs.acs.org/10.1021/acsami.4c04218

Notes

The authors declare no competing financial interest.

■ ACKNOWLEDGMENTS

The authors gratefully acknowledge the financial support from the National Science Foundation (NSF) through the CMMI Award #2028462 and the CAREER Award #2342381. This research was conducted at the Materials Chemistry Laboratory (MCL), the Center for Advanced Construction Materials (CACM), and the Characterization Center for Materials and Biology (CCMB) at the University of Texas at Arlington. The authors acknowledge the support that has made the operations of these laboratories possible. The contents of this paper reflect the views and opinions of the authors, who are responsible for the accuracy of the datasets presented herein, and do not reflect the views and/or policies of the agency, nor do the contents constitute a specification, standard or regulation.

■ REFERENCES

(1) Gao, T.; Shen, L.; Shen, M.; Chen, F.; Liu, L.; Gao, L. Analysis on Differences of Carbon Dioxide Emission from Cement Production and Their Major Determinants. *Journal of Cleaner Production* **2015**, *103*, 160−170.

(2) Concrete Needs to Lose Its Colossal Carbon Footprint. *Nature* **2021**, *597* (7878), 593−594;.

(3) Khan, R. I.; Ashraf, W.; Olek, J. Amino Acids as Performance-Controlling Additives in Carbonation-Activated Cementitious Materials. *Cem. Concr. Res.* **2021**, *147*, 106501.

(4) Mo, L.; Hao, Y.; Liu, Y.; Wang, F.; Deng, M. Preparation of Calcium Carbonate Binders via CO_2 Activation of Magnesium Slag. *Cem. Concr. Res.* **2019**, *121*, 81−90.

(5) Boulos, R. A.; Zhang, F.; Tjandra, E. S.; Martin, A. D.; Spagnoli, D.; Raston, C. L. Spinning up the Polymorphs of Calcium Carbonate. *Sci. Rep* **2014**, *4* (1), 3616.

(6) Ni, M.; Ratner, B. D. Differentiation of Calcium Carbonate Polymorphs by Surface Analysis Techniques - An XPS and TOF-SIMS Study. *Surf. Interface Anal.* **2008**, *40* (10), 1356−1361.

(7) *Fortera: Low-CO2 cement inspired by nature*; https://www.globalcement.com/magazine/articles/1230-fortera-low-co2-cement-inspired-by-nature (accessed 2022−09−21).

(8) Hargis, C. W.; Chen, I. A.; Devenney, M.; Fernandez, M. J.; Gilliam, R. J.; Thatcher, R. P. Calcium Carbonate Cement: A Carbon Capture, Utilization, and Storage (CCUS) Technique. *Materials* **2021**, *14* (11), 2709.

(9) Rodriguez-Blanco, J. D.; Shaw, S.; Benning, L. G. The Kinetics and Mechanisms of Amorphous Calcium Carbonate (ACC) Crystallization to Calcite, via Vaterite. *Nanoscale* **2011**, *3* (1), 265−271.

(10) Konopacka-Łyskawa, D. Synthesis Methods and Favorable Conditions for Spherical Vaterite Precipitation: A Review. *Crystals* **2019**, *9* (4), 223.

(11) Konopacka-Łyskawa, D.; Czaplicka, N.; Łapiński, M.; Kościelska, B.; Bray, R. Precipitation and Transformation of Vaterite Calcium Carbonate in the Presence of Some Organic Solvents. *Materials* **2020**, *13* (12), 2742.

(12) Udrea, I.; Capat, C.; Olaru, E. A.; Isopescu, R.; Mihai, M.; Mateescu, C. D.; Bradu, C. Vaterite Synthesis via Gas-Liquid Route under Controlled pH Conditions. *Ind. Eng. Chem. Res.* **2012**, *51* (24), 8185−8193.

(13) Trushina, D. B.; Bukreeva, T. V.; Kovalchuk, M. V.; Antipina, M. N. CaCO3 Vaterite Microparticles for Biomedical and Personal Care Applications. *Materials Science and Engineering: C* **2014**, *45*, 644−658.

(14) Mori, Y.; Enomae, T.; Isogai, A. Preparation of Pure Vaterite by Simple Mechanical Mixing of Two Aqueous Salt Solutions. *Materials Science and Engineering: C* **2009**, *29* (4), 1409−1414.

(15) Liu, W.; Li, Y.-Q.; Tang, L.-P.; Dong, Z.-J. XRD and 29Si MAS NMR Study on Carbonated Cement Paste under Accelerated Carbonation Using Different Concentration of CO_2. *Mater. Today Commun.* **2019**, *19*, 464−470.

(16) Xu, X.; Guo, H.; Li, M.; Deng, X. Bio-Cementation Improvement via $CaCO_3$ Cementation Pattern and Crystal Polymorph: A Review. *Construction and Building Materials* **2021**, *297*, 123478.

(17) Zou, Z.; Bertinetti, L.; Politi, Y.; Fratzl, P.; Habraken, W. J. E. M. Control of Polymorph Selection in Amorphous Calcium Carbonate Crystallization by Poly(Aspartic Acid): Two Different Mechanisms. *Small* **2017**, *13* (21), 1603100.

(18) Malkaj, P.; Dalas, E. Calcium Carbonate Crystallization in the Presence of Aspartic Acid. *Cryst. Growth Des.* **2004**, *4* (4), 721−723.

(19) Tong, H.; Ma, W.; Wang, L.; Wan, P.; Hu, J.; Cao, L. Control over the Crystal Phase, Shape, Size and Aggregation of Calciumcarbonate via al-Aspartic Acid Inducing Process. *Biomaterials* **2004**, *25*, 3923.

(20) Finney, A. R.; Innocenti Malini, R.; Freeman, C. L.; Harding, J. H. Amino Acid and Oligopeptide Effects on Calcium Carbonate Solutions. *Cryst. Growth Des.* **2020**, *20* (5), 3077−3092.

(21) Montanari, G.; Lakshtanov, L. Z.; Tobler, D. J.; Dideriksen, K.; Dalby, K. N.; Bovet, N.; Stipp, S. L. S. Effect of Aspartic Acid and Glycine on Calcite Growth. *Cryst. Growth Des.* **2016**, *16* (9), 4813−4821.

(22) Karaseva, O. N.; Lakshtanov, L. Z.; Okhrimenko, D. V.; Belova, D. A.; Generosi, J.; Stipp, S. L. S. Biopolymer Control on Calcite Precipitation. *Cryst. Growth Des.* **2018**, *18* (5), 2972−2985.

(23) Štajner, L.; Kontrec, J.; NjegićDžakula, B.; Maltar-Strmečki, N.; Plodinec, M.; Lyons, D. M.; Kralj, D. The Effect of Different Amino Acids on Spontaneous Precipitation of Calcium Carbonate Polymorphs. *J. Cryst. Growth* **2018**, *486*, 71−81.

(24) Tobler, D. J.; Blanco, J. D. R.; Dideriksen, K.; Sand, K. K.; Bovet, N.; Benning, L. G.; Stipp, S. L. S. The Effect of Aspartic Acid and Glycine on Amorphous Calcium Carbonate (ACC) Structure, Stability and Crystallization. *Procedia Earth and Planetary Science* **2014**, *10*, 143−148.

(25) Ropo, M.; Blum, V.; Baldauf, C. Trends for Isolated Amino Acids and Dipeptides: Conformation, Divalent Ion Binding, and Remarkable Similarity of Binding to Calcium and Lead. *Sci. Rep* **2016**, *6* (1), 35772.

(26) Fleisch, H. Bisphosphonates. In *Encyclopedia of Endocrine Diseases*; Martini, L., Ed.; Elsevier: New York, 2004; pp 352−361; DOI: 10.1016/B0-12-475570-4/00197-9.

(27) Lewiecki, E. M. Bisphosphonates for the Treatment of Osteoporosis: Insights for Clinicians. *Ther Adv. Chronic Dis* **2010**, *1* (3), 115−128.

(28) Leadbetter, M. R.; Brown, R. W.; McKenna, M. M. Process for the Preparation of Tetraethyl Methylenebisphosphonate. US5688983A, November 18, 1997; https://patents.google.com/patent/US5688983A/en.

(29) Zhao, Y.; Truhlar, D. G. The M06 Suite of Density Functionals for Main Group Thermochemistry, Thermochemical Kinetics, Noncovalent Interactions, Excited States, and Transition Elements: Two New Functionals and Systematic Testing of Four M06-Class Functionals and 12 Other Functionals. *Theor. Chem. Acc.* **2008**, *120* (1), 215−241.

(30) Lambrakos, S. G.; Huang, L.; Massa, L.; Shabaev, A. *Calculation of IR Spectra Using Density Functional Theory for Nerve-Agent-Sorbent Binding*; Naval Research Lab: Washington, DC, 2019.

(31) Hall, R. J.; Davidson, M. M.; Burton, N. A.; Hillier, I. H. Combined Density Functional, Self-Consistent Reaction Field Model of Solvation. *J. Phys. Chem.* **1995**, *99* (3), 921−924.

(32) Frisch, M. J.; Trucks, G. W.; Schlegel, H. B.; Scuseria, G. E.; Robb, M. A.; Cheeseman, J. R.; Scalmani, G.; Barone, V.; Petersson, G. A.; Nakatsuji, H.; Li, X.; Caricato, M.; Marenich, A.; Bloino, J.; Janesko, B. G.; Gomperts, R.; Mennucci, B.; Hratchian, H. P.; Ortiz, J. V.; Izmaylov, A. F.; Sonnenberg, J. L.; Williams-Young, D.; Ding, F.; Lipparini, F.; Egidi, F.; Goings, J.; Peng, B.; Petrone, A.; Henderson, T.; Ranasinghe, D.; Zakrzewski, V. G.; Gao, J.; Rega, N.; Zheng, G.; Liang, W.; Hada, M.; Ehara, M.; Toyota, K.; Fukuda, R.; Hasegawa, J.; Ishida, M.; Nakajima, T.; Honda, Y.; Kitao, O.; Nakai, H.; Vreven, T.; Throssell, K.; Montgomery, J. A., Jr; Peralta, J. E.; Ogliaro, F.; Bearpark, M.; Heyd, J. J.; Brothers, E.; Kudin, K. N.; Staroverov, V. N.; Keith, T.; Kobayashi, R.; Normand, J.; Raghavachari, K.; Rendell, A.; Burant, J. C.; Iyengar, S. S.; Tomasi, J.; Cossi, M.; Millam, J. M.; Klene, M.; Adamo, C.; Cammi, R.; Ochterski, J. W.; Martin, R. L.; Morokuma, K.; Farkas, O.; Foresman, J. B.; Fox, D. J. *Gaussian 09*; https://gaussian.com.

(33) *Igor Pro*; https://www.wavemetrics.com/software/igor-pro-9.

(34) Nečas, D.; Klapetek, P. Gwyddion: An Open-Source Software for SPM Data Analysis. *Open Physics* **2012**, *10* (1), 181−188.

(35) Partkurst, D. L.; Appelo, C. A. J. *User's Guide to PHREEQC (Version 2): A Computer Program for Speciation, Batch-Reaction, One-Dimensional Transport, and Inverse Geochemical Calculations*; USGS, 1999; DOI: 10.3133/wri994259.

(36) Fukue, M.; Nakamura, T.; Kato, Y. Cementation of Soils Due to Calcium Carbonate. *Soils and Foundations* **1999**, *39* (6), 55−64.

(37) Xie, A.-J.; Shen, Y.-H.; Zhang, C.-Y.; Yuan, Z.-W.; Zhu, X.-M.; Yang, Y.-M. Crystal Growth of Calcium Carbonate with Various Morphologies in Different Amino Acid Systems. *J. Cryst. Growth* **2005**, *285* (3), 436−443.

(38) Chuajiw, W.; Takatori, K.; Igarashi, T.; Hara, H.; Fukushima, Y. The Influence of Aliphatic Amines, Diamines, and Amino Acids on the Polymorph of Calcium Carbonate Precipitated by the Introduction of Carbon Dioxide Gas into Calcium Hydroxide Aqueous Suspensions. *J. Cryst. Growth* **2014**, *386*, 119−127.

(39) Wang, C.; Xiao, P.; Zhao, J.; Zhao, X.; Liu, Y.; Wang, Z. Biomimetic Synthesis of Hydrophobic Calcium Carbonate Nanoparticles via a Carbonation Route. *Powder Technol.* **2006**, *170* (1), 31−35.

(40) Grabenstetter, R. J.; Quimby, O. T.; Flautt, T. J. Acid Dissociation Constants of Substituted Methanediphosphonic Acids. Correlation with Phosphorus-31 Magnetic Resonance Chemical Shift and with Taft Σ*. *J. Phys. Chem.* **1967**, *71* (13), 4194−4202.

(41) Manallack, D. T. The pKa Distribution of Drugs: Application to Drug Discovery. *Perspect Medicin Chem.* **2007**, *1*, 25−38.

(42) Manallack, D. T.; Prankerd, R. J.; Yuriev, E.; Oprea, T. I.; Chalmers, D. K. The Significance of Acid/Base Properties in Drug Discovery. *Chem. Soc. Rev.* **2013**, *42* (2), 485−496.

(43) Chemaxon. *Key Properties in Drug Design | Predicting Lipophilicity, pKa and Solubility*; https://chemaxon.com/blog/presentation/key-properties-in-drug-design-predicting-lipophilicity-pka-and-solubility-0 (accessed 2023−08−01).

(44) Settimo, L.; Bellman, K.; Knegtel, R. M. A. Comparison of the Accuracy of Experimental and Predicted pKa Values of Basic and Acidic Compounds. *Pharm. Res.* **2014**, *31* (4), 1082−1095.

(45) Madaj, R.; Pawlowska, R.; Chworos, A. In Silico Exploration of Binding of Selected Bisphosphonate Derivatives to Placental Alkaline Phosphatase via Docking and Molecular Dynamics. *Journal of Molecular Graphics and Modelling* **2021**, *103*, 107801.

(46) Mukherjee, S.; Huang, C.; Guerra, F.; Wang, K.; Oldfield, E. Thermodynamics of Bisphosphonates Binding to Human Bone: A Two-Site Model. *J. Am. Chem. Soc.* **2009**, *131* (24), 8374−8375.

(47) Liénard, R.; De Winter, J.; Coulembier, O. Cyclic Polymers: Advances in Their Synthesis, Properties, and Biomedical Applications. *J. Polym. Sci.* **2020**, *58* (11), 1481−1502.

(48) Falini, G.; Fermani, S.; Reggi, M.; NjegićDžakula, B.; Kralj, D. Evidence of Structural Variability among Synthetic and Biogenic Vaterite. *Chem. Commun.* **2014**, *50* (97), 15370−15373.

(49) Chakoumakos, B. C.; Pracheil, B. M.; Koenigs, R. P.; Bruch, R. M.; Feygenson, M. Empirically Testing Vaterite Structural Models Using Neutron Diffraction and Thermal Analysis. *Sci. Rep* **2016**, *6* (1), 36799.

(50) Gorna, K.; Hund, M.; Vučak, M.; Gröhn, F.; Wegner, G. Amorphous Calcium Carbonate in Form of Spherical Nanosized Particles and Its Application as Fillers for Polymers. *Materials Science and Engineering: A* **2008**, *477* (1), 217−225.

(51) Karunadasa, K. S. P.; Manoratne, C. H.; Pitawala, H. M. T. G. A.; Rajapakse, R. M. G. Thermal Decomposition of Calcium Carbonate (Calcite Polymorph) as Examined by in-Situ High-Temperature X-Ray Powder Diffraction. *J. Phys. Chem. Solids* **2019**, *134*, 21−28.

(52) Yan, D.; Lu, J.; Sun, Y.; Wang, T.; Meng, T.; Zeng, Q.; Liu, Y. CO2 Pretreatment to Aerated Concrete with High-Volume Industry Wastes Enables a Sustainable Precast Concrete Industry. *ACS Sustainable Chem. Eng.* **2021**, *9* (8), 3363−3375.

(53) Alanne, A.-L.; Hyvönen, H.; Lahtinen, M.; Ylisirniö, M.; Turhanen, P.; Kolehmainen, E.; Peräniemi, S.; Vepsäläinen, J. Systematic Study of the Physicochemical Properties of a Homologous Series of Aminobisphosphonates. *Molecules* **2012**, *17* (9), 10928−10945.

(54) Ihli, J.; Wong, W. C.; Noel, E. H.; Kim, Y.-Y.; Kulak, A. N.; Christenson, H. K.; Duer, M. J.; Meldrum, F. C. Dehydration and Crystallization of Amorphous Calcium Carbonate in Solution and in Air. *Nat. Commun.* **2014**, *5* (1), 3169.

(55) Weiner, S.; Levi-Kalisman, Y.; Raz, S.; Addadi, L. Biologically Formed Amorphous Calcium Carbonate. *Connective Tissue Research* **2003**, *44* (1), 214−218.

(56) Tal, N.; Rudnick-Glick, S.; Grinberg, I.; Natan, M.; Banin, E.; Margel, S. Engineering of a New Bisphosphonate Monomer and Nanoparticles of Narrow Size Distribution for Antibacterial Applications. *ACS Omega* **2018**, *3* (2), 1458−1469.

(57) Huang, S.-C.; Naka, K.; Chujo, Y. A Carbonate Controlled-Addition Method for Amorphous Calcium Carbonate Spheres Stabilized by Poly(Acrylic Acid)s. *Langmuir* **2007**, *23* (24), 12086−12095.

(58) Zou, Z.; Polishchuk, I.; Bertinetti, L.; Pokroy, B.; Politi, Y.; Fratzl, P.; Habraken, W. J. E. M. Additives Influence the Phase Behavior of Calcium Carbonate Solution by a Cooperative Ion-Association Process. *J. Mater. Chem. B* **2018**, *6* (3), 449−457.

(59) Zou, Z.; Bertinetti, L.; Politi, Y.; Jensen, A. C. S.; Weiner, S.; Addadi, L.; Fratzl, P.; Habraken, W. J. E. M. Opposite Particle Size Effect on Amorphous Calcium Carbonate Crystallization in Water and during Heating in Air. *Chem. Mater.* **2015**, *27* (12), 4237−4246.

(60) Furman, B. L. Bisphosphonates. In *xPharm: The Comprehensive Pharmacology Reference*; Enna, S. J., Bylund, D. B., Eds.; Elsevier: New York, 2007; pp 1−3; DOI: 10.1016/B978-008055232-3.61038-4.

(61) Baynton, A.; Chandler, B. D.; Jones, F.; Nealon, G.; Ogden, M. I.; Radomirovic, T.; Shimizu, G. K. H.; Taylor, J. M. Phosphonate Additives Do Not Always Inhibit Crystallization. *CrystEngComm* **2011**, *13* (4), 1090−1095.

(62) Gong, L.; Altman, R. B.; Klein, T. E. Bisphosphonates Pathway. *Pharmacogenet Genomics* **2011**, *21* (1), 50−53.

(63) Rodriguez-Navarro, C.; Burgos Cara, A.; Elert, K.; Putnis, C. V.; Ruiz-Agudo, E. Direct Nanoscale Imaging Reveals the Growth of Calcite Crystals via Amorphous Nanoparticles. *Cryst. Growth Des.* **2016**, *16* (4), 1850−1860.

(64) Ihli, J.; Kim, Y.-Y.; Noel, E. H.; Meldrum, F. C. The Effect of Additives on Amorphous Calcium Carbonate (ACC): Janus Behavior in Solution and the Solid State. *Adv. Funct. Mater.* **2013**, *23* (12), 1575−1585.

(65) Volmer, M.; Weber, A. Keimbildung in übersättigten Gebilden. *Zeitschrift für Physikalische Chemie* **1926**, *119U* (1), 277−301.

(66) Frank, F. C.; Van Der Merwe, J. H.; Mott, N. F. One-Dimensional Dislocations. II. Misfitting Monolayers and Oriented Overgrowth. *Proceedings of the Royal Society of London. Series A. Mathematical and Physical Sciences* **1949**, *198* (1053), 216−225.

(67) Wang, J.; Becker, U. Structure and Carbonate Orientation of Vaterite ($CaCO_3$). *Am. Mineral.* **2009**, *94* (2−3), 380−386.

(68) Ye, S.; Feng, P.; Liu, J. Topographic Analysis of Calcite (104) Cleavage Surface Dissolution in Ethanol-Water Solutions. *Minerals* **2021**, *11* (4), 376.

(69) McDonald, L. J.; Carballo-Meilan, M. A.; Chacartegui, R.; Afzal, W. The Physicochemical Properties of Portland Cement Blended with Calcium Carbonate with Different Morphologies as a Supplementary Cementitious Material. *Journal of Cleaner Production* **2022**, *338*, 130309.

(70) Zhou, Y.; Wu, F.; Jinag, L.; Lu, B.; Hou, G.; Zhu, J. Production of Vaterite via Wet Carbonation of Carbide Residue: Enhancing Cement Properties and CO_2 Sequestration. *Cement and Concrete Composites* **2024**, *150*, 105549.